Energy materials

Monodispersed FeS nanoparticles confined in 3D interconnected carbon nanosheets network as an anode for high-performance lithium-ion batteries

Xuan Miao[1], Haiqiang Li[1], Li Wang[1], Yanli Li[1], Dongfei Sun[1,*] , Xiaozhong Zhou[1], and Ziqiang Lei[1]

[1] *Key Laboratory of Eco-functional Polymer Materials of the Ministry of Education, Key Laboratory of Eco-environmental Polymer Materials of Gansu Province, College of Chemistry and Chemical Engineering, Northwest Normal University, Lanzhou 730070, China*

ABSTRACT

Transition metal sulfides as the most prominent candidates with high theoretical capacities; however, serious agglomeration and enormous volumetric variation limit its application in lithium-ion batteries. Herein, a chemical blowing strategy for the synthesis of FeS nanoparticles encapsulated into 3D porous carbon framework via chemical vapor deposition method and subsequent sulfidation process. In the constructed architecture, the monodispersed FeS nanoparticles are fully encapsulated in graphitic carbon, simultaneously, confined in 3D architecture composed of 2D graphitic carbon nanosheets. The unique architecture provides a facilitated transport pathway, enhances electron conductivity and buffers the volumetric expansion of FeS. Consequently, the composite delivers a high reversible capacity of 1084.2 mAh g^{-1} at 0.1 A g^{-1}, excellent rate capability (723.5 mAh g^{-1} at 1 A g^{-1}), and outstanding cycling stability (a specific capacity of 848.3 mAh g^{-1} without decay is achieved at 0.5 A g^{-1}). Therefore, the present work suggests that the novel design of 3D FeS/C material provides a strategy for achieving high-performance anodes in lithium-ion batteries.

GRAPHIC ABSTRACT

Uniformly monodispersed FeS nanoparticles confined in 3D interconnected carbon network was synthesized by using chemical vapor deposition method and subsequent sulfidation process. The hybrid electrode exhibits excellent performance with a reversible capacity of 1084.2 mAh g^{-1} at 0.1 A g^{-1} as well as outstanding cycling stability performance of 848.3 mAh g^{-1} at 0.5 A g^{-1} after 170 cycles.

Xuan Miao and Haiqiang Li are co-first authors, who contributed equally to this manuscript.

Address correspondence to E-mail: dongfeisun@nwnu.edu.cn

🖄 Springer
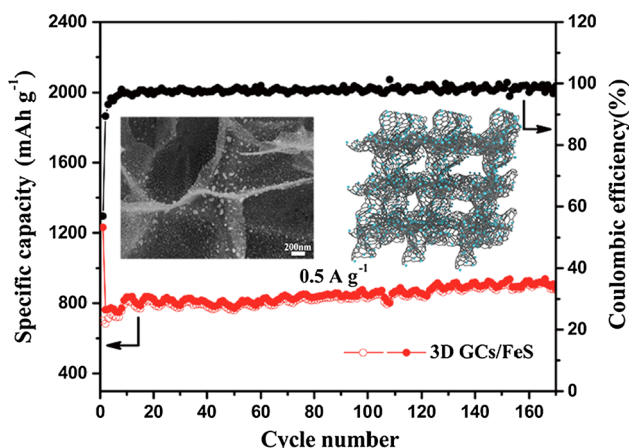
Introduction

New energy technologies, which satisfy the increasing demand for clean and renewable energy, are crucial to promoting energy development [1–4]. Among the available energy storage technologies, rechargeable lithium-ion batteries (LIBs) have been identified as the main power source for various portable electronics. Despite the great advancement, traditional LIBs with graphite anode seem unable to meet the demands of high-energy applications [5]. Exploring high capacity anodes with outstanding rate capability and long lifetimes are of vital importance for the further application of LIBs. In recent years, inorganic host materials (metal oxides and sulfides) often used as active materials to enhance electrochemical performance because of their large theoretical capacity [6–9]. Among those candidates, transition metal sulfides (TMSs) have received more tremendous attention, due to the metal–sulfur bonds are easily broken during the conversion reaction, which is conducive to promote reaction kinetics and improve the lithium storage properties [10–12]. In particular, iron sulfide (FeS) as conversion-type anode material [13], is a potential alternative because of its natural abundance, innoxious, high theoretical capacity (609 mAh g^{-1}), and appropriate reaction voltage with lithium [14]. Unfortunately, similar to its oxide, the enormous volume expansion (< 200%) during the cycling process leads to sluggish kinetics of electrochemical reactions and exceptional capacity

fading [15, 16]. What's more, the formation of polysulfides (Li$_2$S$_x$, 2 < x <8) with the subsequent loss of active material results in the inhibition of the electrode electrochemical reaction [17–19].

To address these issues, one effective strategy is to design the electrode with a nanoscale particle, which can provide more surface for Li$^+$ storage and shorten the Li$^+$ diffusion distance. Moreover, the strategy is also one route to achieve high pseudocapacitance, since the Li$^+$ diffusion distances are greatly shortened. To alleviate the volumetric variations and prevent the aggregation of electrodes, well-dispersing nanoparticles in carbonaceous frameworks, especially graphitic carbon matrix with high electrical conductivity, has been mostly adopted, thus resulting in the improved lithium storage performance [20, 21]. Three-dimensional porous graphitic carbon architecture composed of 2D nanosheets is considered a highly promising skeleton for building stable and fast lithium storage owing to their unique advantageous features, e.g., large surface area, open structure with the surface-exposed actives, good structural stability to prevent stack and aggregation. Employing 3D carbon skeleton to host the TMSs nanoparticles (NPs) could improve the electrochemical performance by increasing the electronic conductivity, confining crystal growth into finite space, and restraining the agglomeration of TMSs NPs [15, 22]. In view of their superiorities, many strategies were proposed to construct TMSs nanoparticles with 3D carbonaceous materials [23, 24]. However, most of TMSs NPs are dispersed on the surface of carbon materials with

weak interaction, leading to the agglomerate together and subsequently capacity fading during the intercalation/extraction process [17]. Based on the above considerations, it is feasible to construct monodispersed TMSs NPs confined in 3D carbon to achieve excellent electrochemical performance in LIBs.

Herein, we have developed a chemical blowing strategy for the synthesis of FeS NPs encapsulated into 3D porous carbon framework via chemical vapor deposition (CVD) method and subsequent sulfidation. The macroporous structure is constructed of interconnected graphitic carbon nanosheets, while the monodispersed FeS NPs are encapsulated in graphitic carbon nanosheets. The novel architecture offers several advantages: (1) The monodispersed FeS NPs prevent them from intermediate contact, thus accommodate the strain and ensure the structural integrity after the cycles. (2) The well-dispersed FeS NPs can also provide sufficient electrode–electrolyte contact areas across the interface and reduce the lithium-ion diffusion length, which significantly promotes the electrochemical kinetics, especially at high current densities. (3) The monodispersed FeS NPs embedded in carbon framework can enhance the electric conductivity, ensuring fast ion/electron transport on FeS. Benefiting from these structural features and dominant surface-controlled capacitive contribution, the composite anode delivers a high reversible capacity of 1084.2 mAh g^{-1} over 100 cycles at 0.1 A g^{-1}, excellent rate performance (723.5 mAh g^{-1} is achieved at high current density 1 A g^{-1}) as well as outstanding cyclic stability.

Experimental section

Synthesis of the 3D GCs/FeS composite

Polyvinylpyrrolidone (PVP-K30, 1.0 g) and Fe(NO$_3$)$_3$·9H$_2$O (1.5 g) were dissolved in 10 mL of deionized water. The mixture solution was kept at 90 °C until fully dried in oil bath pan under stirring. The obtained yellow powder was ground and then first heated under Ar atmosphere at 700 °C for 1 h with a heating rate of 5 °C min^{-1}. Finally, the black powder (3D GCs/Fe) was collected.

To synthesize the 3D GCs/FeS composite, 3D GCs/Fe sample was first calcined under air atmosphere at 300 °C for 3 h to obtain 3D GCs/Fe$_2$O$_3$ sample. Then, the 3D GCs/Fe$_2$O$_3$ sample was mixed with sulfur powder (mass ratio of 1:1.2), annealed from 150 °C for 2 h with a heating rate of 2 °C min^{-1} to 550 °C for 6 h with a heating rate of 5 °C min^{-1} under Ar atmosphere. Finally, the resulting product was labeled as 3D GCs/FeS. For comparison, pristine FeS was also prepared by the same procedures without the addition of PVP.

Structural characterization

Information about the microstructure and morphology of 3D GCs/FeS, 3D GCs/Fe and pristine FeS were obtained by field emission scanning electron microscope (FE-SEM, JEOLJSM-6701F) and transmission electron microscopy (TEM, FEI Tecnai G20). The chemical composition of 3D GCs/FeS was determined by element mapping via EDS spectroscopy analysis. The powder X-ray diffraction (XRD RigakuD/Max 2400) measurement was conducted to study the crystal structure of the 3D GCs/FeS and pristine FeS. A confocal in via micro-Raman spectrometer (from Renishaw) with a 532 nm laser was used to analyze 3D GCs/FeS. The X-ray photoelectron spectroscopy (XPS) measurements were carried out with a PHI-5702 X-ray photoelectron spectrometer using monochromatic aluminum anode X-ray source with Ka radiation. Finally, specific surface area and pore size distribution of 3D GCs/FeS were obtained using the nitrogen adsorption–desorption isotherms (Micromeritics ASAP 2020 volumetric adsorption analyzer) at 77 K.

Electrochemical measurements

To prepare the working electrodes, a slurry was obtained by mixing and stirring the as-prepared product. Carbon black and polyvinylidene fluoride (PVDF) with the mass ratio of 7:2:1 in N-methyl-2-pyrrolidone (NMP), respectively. Then, the slurry was coated onto the Cu foil ($R = 6$ mm) and dried in vacuum at 110 °C for 12 h. The active material was controlled about 0.8 mg cm^{-2}. The electrodes were assembled into coin cells (CR 2032) in an argon-filled glove box by using 1 M LiPF$_6$ in dimethyl carbonate (DMC) and ethylene carbonate (EC) (1:1, v/v) as the electrolyte and metallic Li as the counter. The assembled button cells were tested in the voltage range of 0.01 ∼ 3.0 V (vs. Li$^+$/Li) at various current densities with LAND-CT2001A instruments (Wuhan Jinnuo, China). Cyclic voltammetry (CV) and

electrochemical impedance spectroscopy (EIS) measurements were performed using electrochemistry workstation (Autolab PGSTAT128N, Metrohm, Switzerland).

Results and discussion

The preparation approach of 3D GCs/FeS composite is schematically illustrated in Fig. 1. In the first step, polyvinylpyrrolidone (PVP) and iron nitrate ($Fe(NO_3)_3 \cdot 9H_2O$) were mixed to forming a yellow colloid, follow it was kept at 90 °C until fully dried (as shown in Fig. S1). Then, the adequate mixture was carbonized at 700 °C in an Ar atmosphere. In these steps, the bubble walls were gradually thinned by the combined effect of the gas release, which subsequently could be graphitized into ultrathin carbon sheets with the increasing temperature. Meanwhile, Fe NPs were formed and encapsulated into 3D carbon nanosheets, which could be conducive to obtain the carbon materials with high graphitization degree. During this process, 3D porous carbon skeleton was achieved, which could be ascribed to assistance of the released gas accompanied by the decomposition of $Fe(NO_3)_3$. In the meantime, the carbonaceous material was graphitized into carbon nanosheets at the high temperature. Subsequently, 3D GCs/Fe composite was calcinated at 300 °C in an air atmosphere. Finally, the 3D GCs/FeS sample was obtained by a facile sulfidation process with sulfur powder. With the rational design of 3D GCs/FeS architecture, the stable 3D structure and monodispersed FeS NPs of 3D GCs/FeS composite were expected to achieve remarkable cycle stability in LIBs.

The morphology and nanostructure of as-obtained materials were investigated by scanning electron microscopy (SEM) and transmission electron microscopy (TEM). Figure S2 exhibits that 3D porous carbon network is constituted of interconnected graphitic carbon nanosheets, which is caused by the combination of chemical blowing of PVP and the gas instantaneously released from the decomposition of iron nitrate. Furthermore, the Fe nanoparticles are uniformly embedded in the carbon nanosheets. As shown in Fig. 2a, b, the 3D network maintains integrity and small FeS NPs are uniformly dispersed in carbon nanosheets framework after the sulfurization process. The monodispersed nanoparticles with small diameters contribute to enhance increase the contact areas between the electrolyte and the electrode. In contrast, pristine FeS consists of particles with hundreds of nanometers (Fig. S3). The energy dispersive X-ray spectroscopy (EDS) mapping (Fig. 2c) further confirms the coexistence of C, Fe and S elements in 3D GCs/FeS, as well as Fe and S elements uniformly distributed on the surface of carbon nanosheets. And the mass content of C elements in the composite could be established as 39.7 wt%
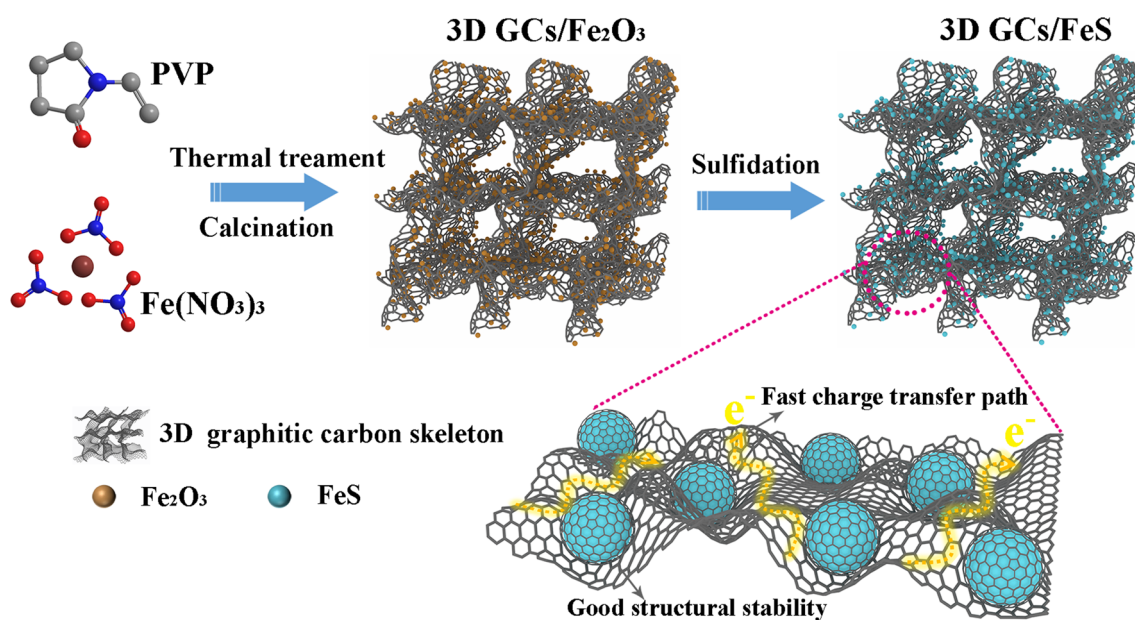

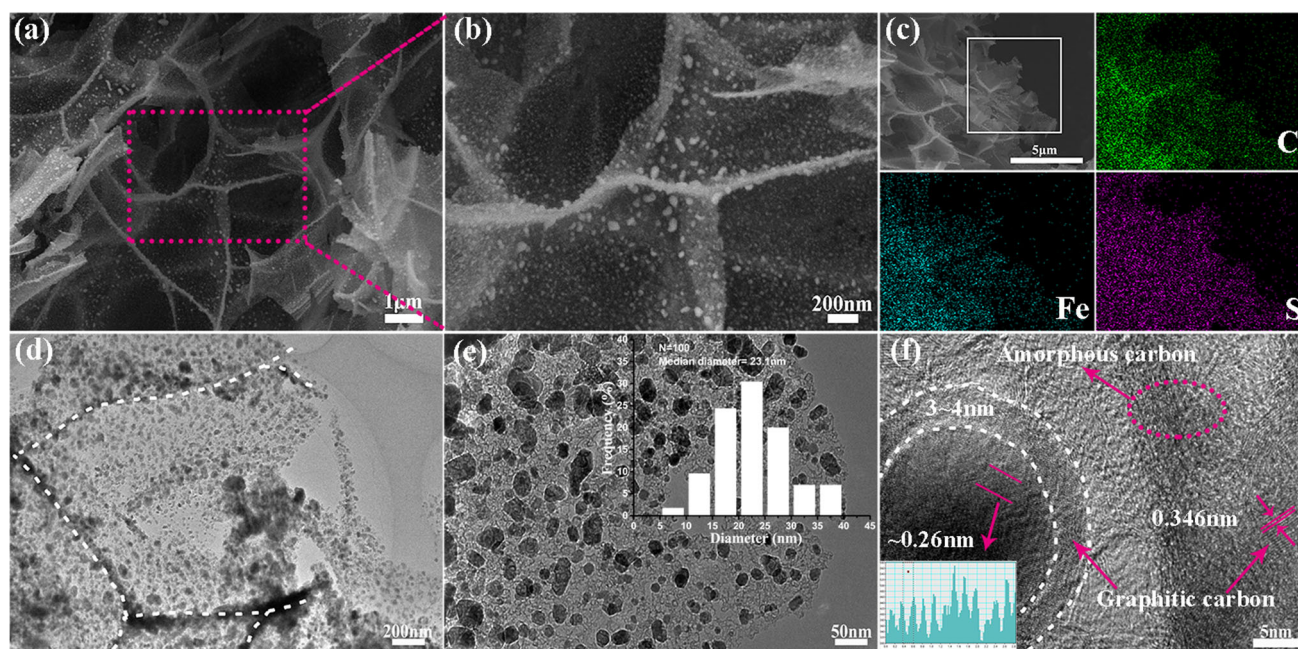**Figure 1** Schematic illustration for preparing 3D GCs/FeS composite.

Figure 2 Morphological and structural characteristics of the 3D GCs/FeS composite. **a**, **b** SEM images, **c** EDS elemental mapping images, and **d**, **e**, **f** TEM and HRTEM images of the 3D GCs/FeS.

(Fig. S4). Figure 2d–f shows the TEM images of 3D GCs/FeS. Figure 2d clearly demonstrates the interconnected graphitic carbon nanosheets to form three-dimensional architecture. FeS NPs with the average diameter of 23.1 nm are uniformly anchored on the surface of carbon nanosheets, and many nanopores on the carbon nanosheets (Fig. 2e). The high-resolution TEM (HRTEM) image reveals that the FeS NPs are entrapped within a thin carbon layer with the approximate thickness of 3–4 nm, which inhibits direct-contact between adjacent FeS NPs and can effectively accommodate the volume expansion of FeS NPs (Fig. 2f) [25, 26]. Furthermore, the HRTEM image also shows clear lattice fringes of ~ 0.26 nm, which corresponds to the (203) plane belonging to pristine FeS. Meanwhile, it is clearly observed that the outer shell is graphitic carbon with the typical *d*-spacing of 0.346 nm corresponding to the C (002) planes, attributing to the catalysis of metal salt at high temperature.

The XRD characterization was utilized to analyze the phase composition of 3D GCs/FeS (Fig. 3a). The distinct diffraction peak at 25.7° corresponds to the (002) plane of graphitic carbon, the interlayer spacing calculated from Bragg's Law is 0.34 nm, which is inconsistent with the TEM result. The other peaks can be indexed to hexagonal FeS (JPCDS no. 25-0411) [27]

and no other peak appears, indicating the successful fabrication and the high purity of the 3D GCs/FeS. No peak of Fe or Fe_2O_3 is observed, indicating that they were all transformed into FeS [22, 28]. It can be concluded that metal oxide precursor or metal per-oxidation is significant for the preparation of pure metallic sulfide phase [22, 28, 29]. Raman spectrum was further investigated to study the existence of graphitic carbon (Fig. 3b). Two distinct peaks at 1348.8 (D-band) and 1587.4 cm^{-1} (G-band) of carbon can be assigned to amorphous and crystalline graphite, respectively [30]. The large I_D/I_G intensity ratio (1.17) indicates that there are abundant defects on the surface of graphitic carbon, which is presumably beneficial for facilitating the insertion and transfer of Li^+ [17, 31]. The Brunauer–Emmett–Teller (BET) measurement (Fig. 3c) suggested a mesoporous structure for the sample, as evidenced by the type IV profile with an obvious hysteresis loop [32]. The BET specific surface area of 3D GCs/FeS is 228.8 $m^2\ g^{-1}$. Moreover, there are plentiful open mesopores between 2.5 and 35 nm in 3D GCs/FeS. The hierarchical porous characteristic of 3D GCs/FeS is conducive to the penetration of electrolyte and rapid ionic diffusion during the ion insertion/extraction processes.
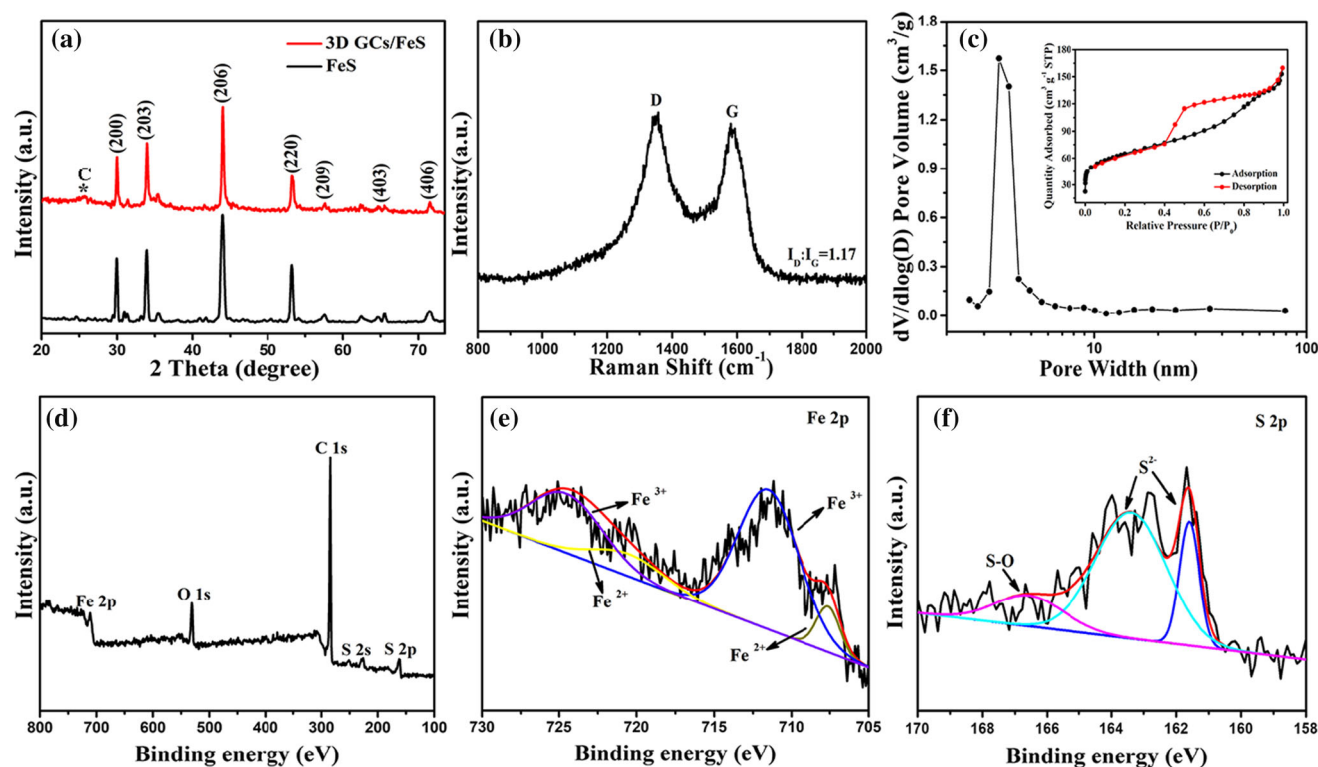
Figure 3 a XRD pattern of 3D GCs/FeS and FeS, **b** Raman spectra and **c** the pore size distribution and nitrogen adsorption–desorption isotherms (inset) of the 3D GCs/FeS, **d, e, f** XPS spectra of as-prepared 3D GCs/FeS: **d** survey spectrum and high-resolution detail spectra of **e** Fe 2p and **f** S 2p regions.

The detailed elemental compositions of 3D GCs/FeS were characterized in detail by X-ray photoelectron spectroscopy (XPS) measurement. The characteristic peaks of Fe 2p, S 2p, C 1s, and O 1s could be distinctly identified from the survey XPS spectrum (Fig. 3d). For the Fe 2p XPS signal (Fig. 3e), the characteristic peaks at 707.6, 711.5, 720.5, and 724.5 eV were confirmed. Two peaks at 707.6 eV and 720.5 eV were ascribed to the Fe^{2+} states in the Fe 2p spectrum of the FeS phase, while the other peaks were ascribed to the Fe^{3+} states because of the high reactivity of FeS toward oxygen [33–35]. The S 2p spectrum (Fig. 3f) had two distinct peaks at 161.6 eV and 163.4 eV, which were attributed to S^{2-}, simultaneously, the bonding of sulfur with oxygen (S–O bond) was supported by the peaks centered at 166.5 eV [36]. The C 1s spectra of 3D GCs/FeS (Fig. S5a) were fitted as three peaks located at 284.7 eV (C–C), 285.6 eV (C–O), and 288.4 eV (C=O) [37, 38]. The XPS survey is also consistent with the Raman and XRD results. The O 1s spectrum (Fig. S5b) exhibits three characteristic peaks located at 530 eV, 531.6 eV, 532.8 eV, and 536.0 eV corresponding Fe–

O, C–O, O–C=O functional groups and H_2O, respectively [33, 39]. The presence of Fe–O proves that there is an interaction between FeS and carbon nanosheet in the materials [33]. The presence of O 1s can be ascribed to polymer-derived carbons contains a certain amount of oxygen [40, 41]. According to EDS analysis (Fig. S4), the mass content of O elements in the composite could be established as 3.69 wt%, which can enhance the wettability of the electrode [20, 42].

The electrochemical properties of pristine FeS and 3D GCs/FeS composite were investigated by cyclic voltammetry (CV). Figure 4a displays the CV curves of 3D GCs/FeS during the initial fifth cycles at a scan rate of 0.2 mV s^{-1} in the voltage window of 0.01–3 V. During the first cathodic scan, two reduction peaks located at 0.95 V and 0.48 V are associated with the conversion reactions from FeS to Li_2S (FeS + 2Li$^+$ + 2e$^-$ → Li_2S + Fe) and related to the formation of solid-electrolyte interphase (SEI) layers, respectively [18, 27]. During the initial anode scan, one oxidation peak at 2.00 V associated with the oxidation reaction of Fe to Li_2FeS_2 (Fe + 2Li$_2$S → Li_2FeS_2 + 2Li$^+$ + 2e$^-$)
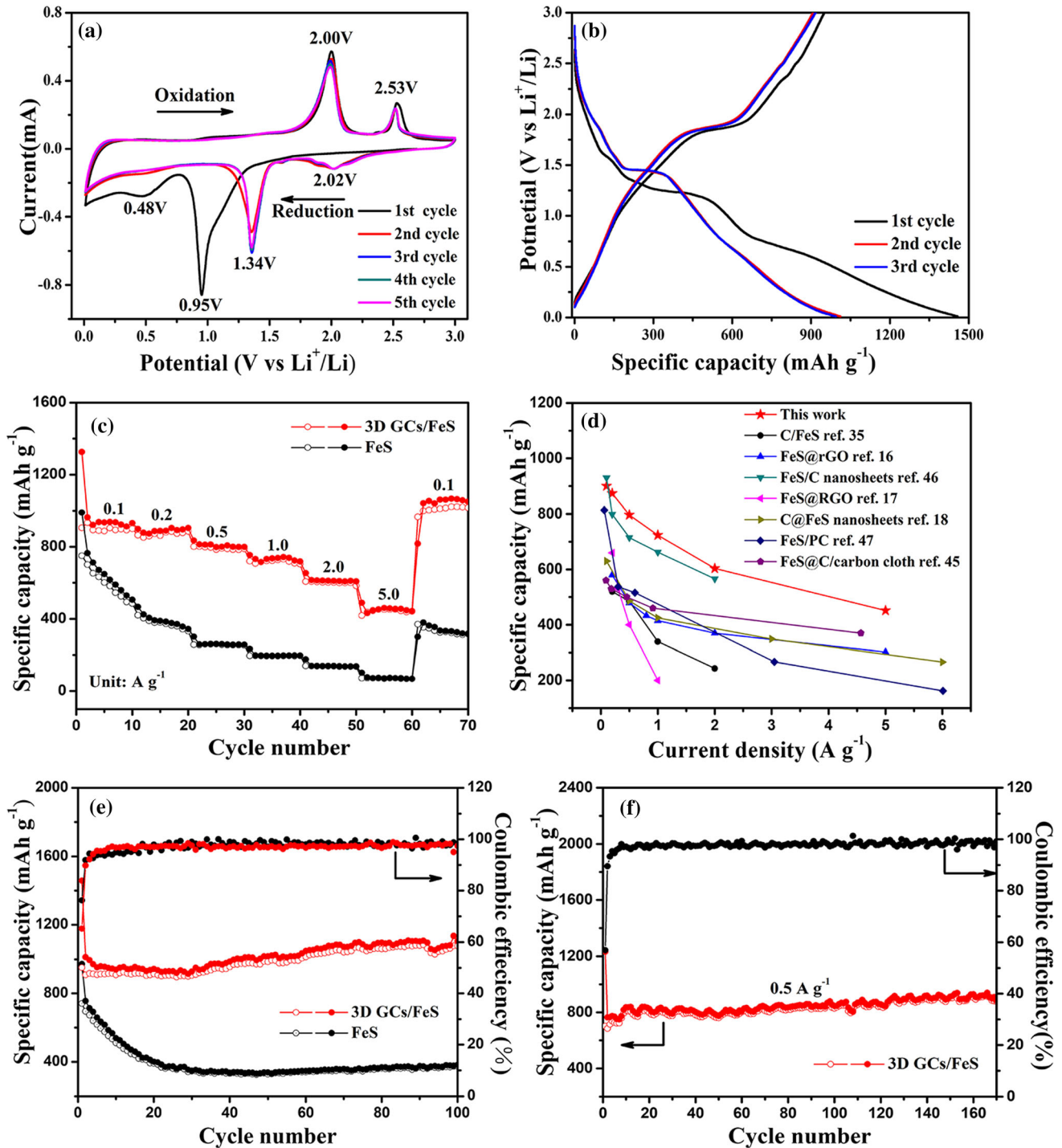
Figure 4 a Cyclic voltammetry curves and **b** galvanostatic charge–discharge curves of the 3D GCs/FeS electrode, **c** rate performance of the 3D GCs/FeS and FeS, **d** a comparison of the rate performance of 3D GCs/FeS with other FeS-based anode materials of LIBs, **e** cycling performances at 0.1 A g^{-1} and **f** long-term cycle performances at 0.5 A g^{-1} of the 3D GCs/FeS.

[30], and the peak at 2.53 V correspond to the formation of Li$_{2-x}$FeS$_2$ (Li$_2$FeS$_2$ → Li$_{2-x}$FeS$_2$ + xLi$^+$ + xe^-) [30, 38, 43]. In the second and subsequent cycles, the novel reduction peaks located at 2.02 and

1.34 V attributed to a new reaction which Li$_{2-x}$FeS$_2$ transferred to Li$_2$FeS$_2$ and then continued lithiation (Li$_2$FeS$_2$ + 2Li → Fe + 2Li$_2$S) [16]. The subsequent oxidation peaks were almost overlapping, suggesting

an excellent electrochemical reversibility of 3D GCs/FeS. In contrast, the cathodic/anodic peaks in the CV curve of FeS were obvious area loss for the successive cycles, indicating the poor cycling reversibility of the pristine FeS sample (Fig. S6a).

Figure 4b shows the typical discharge/charge profiles of the first three of 3D GCs/FeS electrode at 0.1 A g^{-1}. 3D GCs/FeS electrode exhibited initial discharge/charge capacities of 1457.7/950.8 mAh g^{-1} with an initial Coulombic efficiency of 65.2%, the apparent decrease in charge capacity resulted from the formation of SEI film and irreversible generation of Li$_2$S [18, 44]. In comparison, FeS electrode showed initial discharge/charge capacities of 971.9/740.2 mAh g^{-1} (Fig. S6b). The consequence thanks to the robust 3D carbon matrix modification on FeS NPs, which could effectively avoid the direct contact between FeS NPs and electrolyte to reduce the decomposition of electrolyte. In the subsequent cycles, the discharge/charge curves were almost overlapping, indicating the good reversibility. Moreover, the stable plateaus at 1.42 V (during the discharge process) and 1.91 V (during the charging process) were well-consistent with the CV results. 3D GCs/FeS clearly exhibited an attractive rate performance (Fig. 4c). The average discharge capacities of 3D GCs/FeS electrode were 900.4, 873.4, 796.4, 723.5, 603.3, and 451.4 mAh g^{-1} from 0.1 to 5.0 A g^{-1}, respectively. When the current density returns to 0.1 A g^{-1}, the reversible capacity can rapidly recover to 1014.3 mAh g^{-1}. For comparison, the capacities of the pristine FeS at the same rate are only 617.4, 388.6, 260.7, 196.4, 137.8, and 72.2 mAh g^{-1} respectively. Moreover, the rate performance of 3D GCs/FeS electrode is much better than most of the previous studies on FeS-based anodes for LIBs (Fig. 4d) [16–18, 35, 45–47]. 3D GCs/FeS electrode also exhibited excellent cycling performance at 0.1 A g^{-1} (Fig. 4e). The 3D GCs/FeS electrode showed much higher reversible capacity and better cycling performance than FeS electrode. Especially, 3D GCs/FeS electrode can maintain the reversible capacity of 1084.2 mAh g^{-1} over 100 cycles, while the FeS electrode only held the reversible capacity of 374.4 mAh g^{-1} after 100 cycles. Impressively, even at a high current rate of 0.5 A g^{-1} (Fig. 4f), 3D GCs/FeS electrode still demonstrated long-term cycling stability, and the reversible capacity of 848.3 mAh g^{-1} was maintained even after 170 cycles, corresponding to coulombic efficiency

approaching 100% from the fifth to the 170th cycle. The high capacitance derive from the structure advantages of 3D GCs/FeS: the continuous porous carbon framework synergistically with monodispersed FeS nanoparticles form a 3D interconnect cyberspace, which not only provide adequate pathways for achieving fast electron/ion transfer, but also furnish much more storage sites of Li$^+$. Those results indicate that 3D porous carbon skeleton effectively improves Li$^+$ and electron transport kinetics during the discharge/charge process.

In order to better understand the excellent rate performance of the 3D GCs/FeS electrode, the kinetics were studied by CV measurements. The CV curves at different scan rates from 0.2 to 2.0 mV s^{-1} with similar shape are shown in Fig. 5a and Fig. S6c. Apparently, peak current (i) and scan rate (V) are related by the following equation [33]: $i = av^b$ (a and b are the variable parameter). A b value of 0.5 or 1.0 manifests an ideal diffusion-dominated process or a surface determined capacitive-controlled behavior, respectively [48, 49]. The value of b is measured from the slope of log i versus log v. Figure 5b displays the log i versus log v plot of four peaks, the b-values are 0.98, 0.64, 0.70, and 0.72 for 3D GCs/FeS, respectively. Consequently, it suggests that both diffusion-limited charge storage and capacitive behavior contribute to the observed capacities, which leads to fast Li$^+$ insertion/extraction [48]. Furthermore, the more precise percentage of capacitive contributions can be quantified by dividing the current response (i) at a fixed potential (v) for diffusion-controlled reaction ($k_2v^{1/2}$) and capacitive effect (k_1v) can be obtained using the following equation [49, 50]: $i(V) = k_1v + k_2v^{1/2}$. The portion of the current from diffusion-controlled and capacitance capacity can be identified according to both the k_1 and k_2 constants. Figure 5c shows the typical voltage profile for the capacitive current (green region) in comparison with the total current. A dominating capacitive contribution ($\sim$ 83.3%) at 0.8 mV s^{-1} obtained for the 3D GCs/FeS electrode. With the increase in scan rate, the percentage of capacity contribution enlarged gradually with a maximum value of $\sim$ 87.9% at 2.0 mV s^{-1} (Fig. 5d). These results clearly demonstrate that the high pseudocapacitive contribution in the 3D GCs/FeS electrode allows the ultrafast Li$^+$ diffusion, leading to the excellent rate performance in LIBs.

The underlying reason for 3D GCs/FeS electrode with excellent electrochemical performances can be
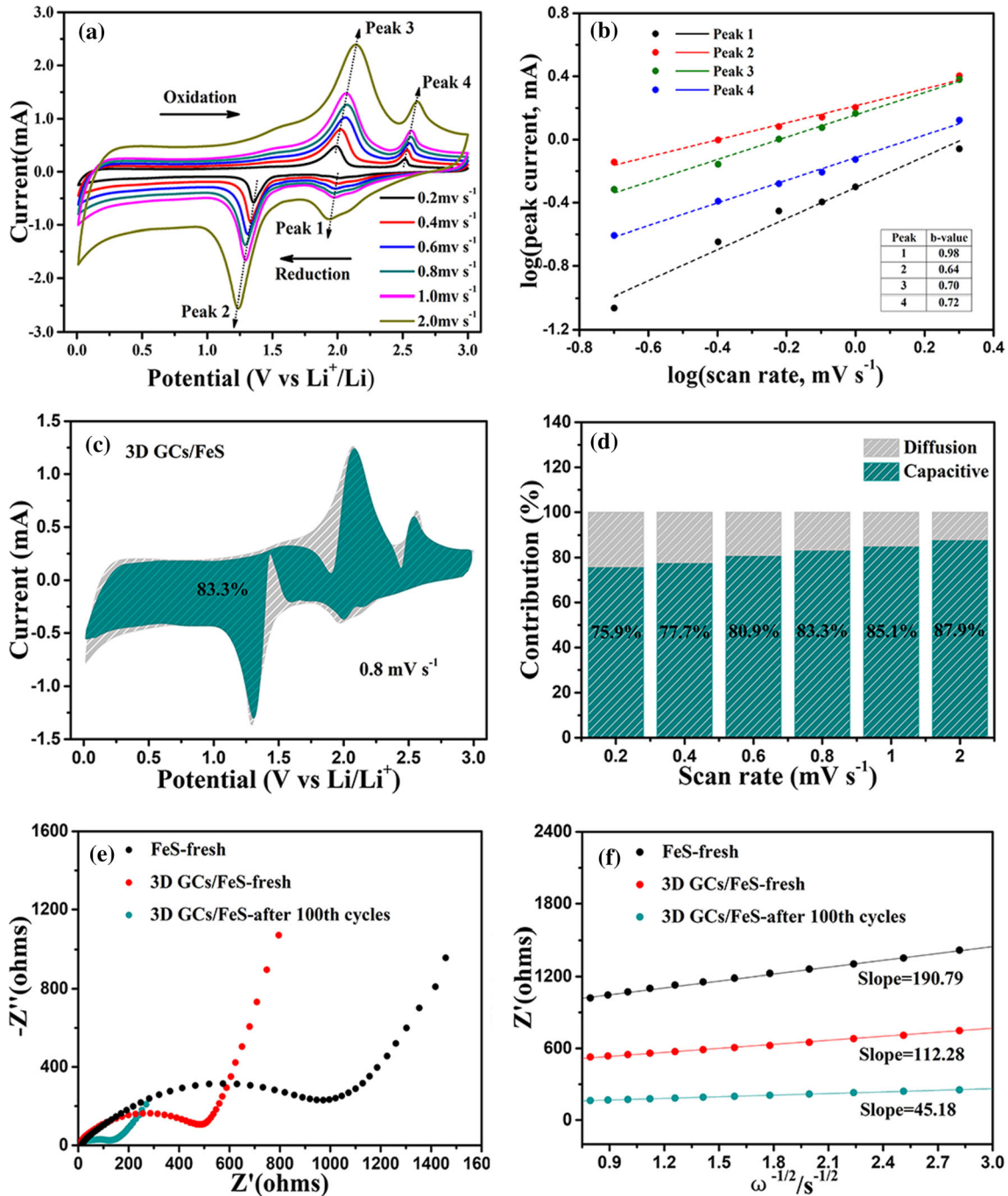
Figure 5 Kinetics and quantitative analysis for the 3D GCs/FeS electrode. **a** CV curves at different scan rates, **b** relation between logarithm peak current and logarithm scan rates, **c** capacitive and diffusive contributions to charge storage at 0.8 mV s^{-1}, **d** percentage of the pseudocapacitive contribution to the overall recorded capacity as a function of the applied scan rate, ranging from 0.2 to 2.0 mV s^{-1}, **e** EIS spectra and **f** relation of $Z' - \omega^{-1/2}$ curves in the low-frequency region of the FeS, fresh 3D GCs/FeS, and 3D GCs/FeS (after 100 cycles at 0.1 A g^{-1}) electrodes.

verified by electrochemical impedance spectroscopy (EIS) measurement (Fig. 5e), and the equivalent circuit diagram are shown in Fig. S7. It is well-known that a large semicircle indicates high charge transfer resistance (R_{ct}) [50, 51], the R_{ct} of the 3D GCs/FeS was 492.6 Ω, which is lower than that of the pristine FeS (984.9 Ω). The result confirms the remarkably enhanced kinetics of electronic transportation

provided by the architecture of 3D GCs/FeS electrode. Simultaneously, the R_{ct} of the 3D GCs/FeS electrode decreases to 148.3 Ω after the 100 cycles, exhibiting a facilitated transfer for electrons/ions at the electrode interface. Additionally, the ion transport can also be investigated according to the Warburg factor(s) related to the slope of the linear fittings in the low-frequency region. From the $Z' - \omega^{-1/2}$ ($\omega = 2\pi f$) curves [50, 52] presented in Fig. 5f, the 3D GCs/FeS electrode exhibits an obviously lower slope than that of pristine FeS, illustrating the faster interface kinetics. Also, the lower slope of the 3D GCs/FeS electrode after 100th cycle further attesting its fast charge transfer and efficient Li^+ insertion/desertion. These results directly confirm that the unique structural feature of 3D GCs/FeS greatly enhances the charge transfer kinetics.

Conclusion

In conclusion, this work reported a facile preparation of 3D porous graphitic carbon/FeS composite by chemical vapor deposition (CVD) method and subsequent sulfidation. As a result, the monodispersed FeS nanoparticles are fully encapsulated in graphitic carbon, simultaneously, confined in 3D architecture composed of 2D graphitic carbon nanosheets. The combination of the 3D porous carbon framework with monodisperse FeS nanoparticles greatly enhance the electrons/ions transport kinetics and improve the surface pseudocapacitive contribution. On the other hand, the continuous 3D porous carbon framework possesses robust mechanical architectures, which can maintain structural integrity and ensure good cyclic stability. Based on those advantages, 3D GCs/FeS electrode simultaneously delivers a high reversible capacity of 1084.2 mAh g^{-1} at 0.1 A g^{-1}, excellent rate capability (723.5 mAh g^{-1} at 1 A g^{-1}), and good cycling stability (a specific capacity of 848.3 mAh g^{-1} without decay is achieved at 0.5 A g^{-1} after 170 cycles), indicating its potential for LIB applications.

Acknowledgements

Compliance with ethical standards

Conflict of interest The authors declare that they have no known competing financial interests or personal relationships that could have appeared to influence the work reported in this paper.

Electronic supplementary material: The online version of this article (https://doi.org/10.1007/s108 53-020-04843-9) contains supplementary material, which is available to authorized users.

References

[1] Li M, Lu J, Chen ZW, Amine K (2018) 30 years of lithium-ion batteries. Adv Mater 30:1800561

[2] He JR, Chen YF, Manthiram A (2019) Metal sulfide-decorated carbon sponge as a highly efficient electrocatalyst and absorbant for polysulfide in high-loading Li_2S batteries. Adv Energy Mater 9:1900584

[3] He JR, Hartmann G, Lee M, Hwang GS, Chen YF, Manthiram A (2019) Freestanding 1T MoS_2/graphene heterostructures as a highly efficient electrocatalyst for lithium polysulfides in Li–S batteries. Energy Environ Sci 12:344–350

[4] Yu B, Chen YF, Wang ZG, Chen DJ, Wang XQ, Zhang WL et al (2020) 1T-MoS_2 nanotubes wrapped with N-doped graphene as highly-efficient absorbent and electrocatalyst for Li–S batteries. J Power Sources 447:227364

[5] He JR, Li PJ, Lv WQ, Wen K, Chen YF, Zhang WL et al (2016) Three-dimensional hierarchically structured aerogels constructed with layered MoS_2/graphene nanosheets as free-standing anodes for high-performance lithium ion batteries. Electrochim Acta 215:12–18

[6] He JR, Li Q, Chen YF, Xu C, Zhou K, Wang XQ et al (2017) Self-assembled cauliflower-like FeS_2 anchored into graphene foam as free-standing anode for high-performance lithium-ion batteries. Carbon 114:111–116

[7] Qi F, He JR, Chen YF, Zheng BJ, Li Q, Wang XQ et al (2017) Few-layered ReS_2 nanosheets grown on carbon nanotubes: a highly efficient anode for high-performance lithium-ion batteries. Chem Eng J 315:10–17

[8] Xu C, Jing Y, He JR, Zhou K, Chen YF, Li Q et al (2017) Self-assembled interwoven CoS_2/CNTs/graphene

architecture as anode for high-performance lithium ion batteries. J Alloys Compd 708:1178–1183

[9] Li Q, Chen YF, He JR, Fu F, Lin J, Zhang WL (2016) Three-dimensional VS$_4$/graphene hierarchical architecture as high-capacity anode for lithium-ion batteries. J Alloys Compd 685:294–299

[10] Hu X, Liu YJ, Chen JX, Jia JC, Zhan HB, Wen ZH (2019) FeS quantum dots embedded in 3D ordered macroporous carbon nanocomposite for high-performance sodium-ion hybrid capacitors. J Mater Chem A 7:1138–1148

[11] Qi F, Chen YF, Zheng BJ, He JR, Li Q, Wang XQ et al (2017) Hierarchical architecture of ReS$_2$/rGO composites with enhanced electrochemical properties for lithium-ion batteries. Appl Surf Sci 413:123–128

[12] Qi F, Chen YF, Zheng BJ, He JR, Li Q, Wang XQ et al (2017) 3D chrysanthemum-like ReS$_2$ microspheres composed of curly few-layered nanosheets with enhanced electrochemical properties for lithium-ion batteries. J Mater Sci 52:3622–3629

[13] Xie J, Carrasco J, Li RR, Shen HJ, Chen Q, Yang MH (2019) Novel 3D flower-like micro/nano-structure FeS/N-doped-C composites as advanced cathodes with high lithium storage performances. J Power Sources 431:226–231

[14] Zhu CB, Wen YR, van Aken PA, Maier J, Yu Y (2015) High lithium storage performance of FeS nanodots in porous graphitic carbon nanowires. Adv Funct Mater 25:2335–2342

[15] Haridas AK, Jeon J, Heo J, Liu Y, Saroha R, Joo JH et al (2019) In-situ construction of iron sulfide nanoparticle loaded graphitic carbon capsules from waste biomass for sustainable lithium-ion storage. ACS Sustain Chem Eng 7:6870–6879

[16] Huang MB, Xu A, Duan HH, Wu SP (2018) Enhanced pseudocapacitance contribution to outstanding Li-storage performance for a reduced graphene oxide-wrapped FeS composite anode. J Mater Chem A 6:7155–7161

[17] Fei L, Lin QL, Yuan B, Chen G, Xie P, Li YL et al (2013) Reduced graphene oxide wrapped FeS nanocomposite for lithium-ion battery anode with improved performance. ACS Appl Mater Interfaces 5:5330–5335

[18] Xu C, Zeng Y, Rui XH, Xiao N, Zhu JX, Zhang WY et al (2012) Controlled soft-template synthesis of ultrathin C@FeS nanosheets with high-Li-storage performance. ACS Nano 6:4713–4721

[19] He JR, Chen YF, Manthiram A (2018) Vertical Co$_9$S$_8$ hollow nanowall arrays grown on a Celgard separator as a multifunctional polysulfide barrier for high-performance Li–S batteries. Energy Environ Sci 11:2560–2568

[20] Ma Y, Ma YJ, Kim GT, Diemant T, Behm RJ, Geiger D et al (2019) Superior lithium storage capacity of α-MnS

nanoparticles embedded in S-doped carbonaceous mesoporous frameworks. Adv Energy Mater 9:1902077

[21] He JR, Chen YF, Li PJ, Fu F, Wang ZG, Zhang WL (2015) Self-assembled CoS$_2$ nanoparticles wrapped by CoS$_2$-quantum-dots-anchored graphene nanosheets as superior-capability anode for lithium-ion batteries. Electrochim Acta 182:424–429

[22] Wang QH, Zhang WC, Guo C, Liu YJ, Wang C, Guo ZP (2017) In situ construction of 3D interconnected FeS@Fe$_3$C@graphitic carbon networks for high-performance sodium-ion batteries. Adv Funct Mater 27:1703390

[23] Bu FX, Xiao PT, Chen JD, Aly Aboud MF, Shakir I, Xu YX (2018) Rational design of three-dimensional graphene encapsulated core–shell FeS@carbon nanocomposite as a flexible high-performance anode for sodium-ion batteries. J Mater Chem A 6:6414–6421

[24] Li JS, Xu XJ, Yu XT, Han X, Zhang T, Zuo Y et al (2020) Monodisperse CoSn and NiSn nanoparticles supported on commercial carbon as anode for lithium- and potassium-ion batteries. ACS Appl Mater Interfaces 12:4414–4422

[25] Xu L, Hu YJ, Zhang HX, Jiang H, Li CZ (2016) Confined synthesis of FeS$_2$ nanoparticles encapsulated in carbon nanotube hybrids for ultrastable lithium-ion batteries. ACS Sustain Chem Eng 4:4251–4255

[26] Su QF, Lu YH, Liu SH, Zhang XC, Lin YH, Fu RW, Wu DC (2018) Nanonetwork-structured yolk-shell FeS$_2$@C as high-performance cathode materials for Li-ion batteries. Carbon 140:433–440

[27] Chen SH, Fan L, Xu LL, Liu Q, Qin Y, Lu BG (2017) 100 K cycles: core-shell H-FeS@C based lithium-ion battery anode. Energy Storage Mater 8:20–27

[28] Wang QH, Guo C, Zhu YX, He JP, Wang HQ (2018) Reduced graphene oxide-wrapped FeS$_2$ composite as anode for high-performance sodium-ion batteries. Nano Micro Lett 10:30–38

[29] Jia HN, Wang ZY, Zheng XH, Cai YF, Lin JH, Liang HY et al (2019) Controlled synthesis of MOF-derived quadruple-shelled CoS$_2$ hollow dodecahedrons as enhanced electrodes for supercapacitors. Electrochim Acta 312:54–61

[30] Xu YX, Li WY, Zhang F, Zhang XL, Zhang WJ, Lee CS, Tang YB (2016) In situ incorporation of FeS nanoparticles/carbon nanosheets composite with an interconnected porous structure as a high-performance anode for lithium ion batteries. J Mater Chem A 4:3697–3703

[31] Hu X, Liu Y, Li J, Wang G, Chen J, Zhong G et al (2020) Self-assembling of conductive interlayer-expanded WS$_2$ nanosheets into 3D hollow hierarchical microflower bud hybrids for fast and stable sodium storage. Adv Funct Mater 30:1907677

[32] Fan HH, Li HH, Guo JZ, Zheng YP, Huang KC, Fan CY et al (2018) Target construction of ultrathin graphitic carbon encapsulated FeS hierarchical microspheres featuring superior low-temperature lithium/sodium storage properties. J Mater Chem A 6:7997–8005

[33] Hou BH, Wang YY, Guo JZ, Ning QL, Xi XT, Pang WL et al (2018) Pseudocapacitance-boosted ultrafast Na storage in a pie-like FeS@C nanohybrid as an advanced anode material for sodium-ion full batteries. Nanoscale 10:9218–9225

[34] Cho JS, Park JS, Kang YC (2016) Porous FeS nanofibers with numerous nanovoids obtained by Kirkendall diffusion effect for use as anode materials for sodium-ion batteries. Nano Res 10:897–907

[35] Zhao JF, Syed JA, Wen XM, Lu HB, Meng XK (2019) Green synthesis of FeS anchored carbon fibers using egg-shell membrane as a bio-template for energy storage application. J Alloys Compd 777:974–981

[36] Li DH, Sun YY, Chen S, Yao JY, Zhang YH, Xia YZ, Yang DJ (2018) Highly porous FeS/carbon fibers derived from Fe-carrageenan biomass: high-capacity and durable anodes for sodium-ion batteries. ACS Appl Mater Interfaces 10:17175–17182

[37] Yao YY, Zheng JC, Gong ZY, Ding ZY, Zhang J, Yu WJ et al (2019) Metal-organic framework derived flower-like FeS/C composite as an anode material in lithium-ion and sodium-ion batteries. J Alloys Compd 790:288–295

[38] Xu QT, Xue HG, Guo SP (2018) Facile preparation of FeS@GO and its outstanding electrochemical performances for lithium storage. Inorg Chem Front 5:2540–2545

[39] Liu XG, Wu YY, Li XL, Yu JY, Sun YP (2018) FeS@onion-like carbon nanocapsules embedded in amorphous carbon for the lithium ion batteries with excellent cycling stability. Ceram Int 44:13654–13661

[40] Miao X, Sun DF, Zhou XZ, Lei ZQ (2019) Designed formation of nitrogen and sulfur dual-doped hierarchically porous carbon for long-life lithium and sodium ion batteries. Chem Eng J 364:208–216

[41] Sun DF, Yang J, Yan XB (2015) Hierarchically porous and nitrogen, sulfur-codoped graphene-like microspheres as a high capacity anode for lithium ion batteries. Chem Commun 51:2134–2137

[42] Ouyanga T, Zhang TY, Wang HZ, Yang F, Yan J, Zhu K et al (2018) High-throughput fabrication of porous carbon by chemical foaming strategy for high performance supercapacitor. Chem Eng J 352:459–468

[43] Wu B, Song HH, Zhou JS, Chen XH (2011) Iron sulfide-embedded carbon microsphere anode material with high-rate performance for lithium-ion batteries. Chem Commun 47:8653–8655

[44] Shi LD, Li DZ, Yu JL, Liu HC, Zhao Y, Xin HL et al (2018) Uniform core–shell nanobiscuits of Fe_7S_8@C for lithium-ion and sodium-ion batteries with excellent performance. J Mater Chem A 6:7967–7976

[45] Wei X, Li W, Shi J, Gu L, Yu Y (2015) FeS@C on carbon cloth as flexible electrode for both lithium and sodium storage. ACS Appl Mater Interfaces 7:27804–27809

[46] Zhao JG, Hu Z, Sun DZ, Jia H, Liu XM (2019) MOF-derived FeS/C nanosheets for high performance lithium ion batteries. Nanomaterials 9:492–502

[47] Guo SP, Li JC, Ma Z, Chi Y, Xue HG (2016) A facile method to prepare FeS/porous carbon composite as advanced anode material for lithium-ion batteries. J Mater Sci 52:2345–2355

[48] Guo KK, Xi BJ, Wei RC, Li HB, Feng JK, Xiong SL (2020) Hierarchical microcables constructed by CoP@C ⊂ carbon framework intertwined with carbon nanotubes for efficient lithium storage. Adv Energy Mater. https://doi.org/10.1002/aenm.201902913

[49] Sun DF, Miao X, He YJ, Wang L, Zhou XZ, Ma GF, Lei ZQ (2019) 3D interconnected porous graphitic carbon@MoS_2 anchored on carbonized cotton cloth as an anode for enhanced lithium storage performance. Electrochim Acta 320:134616

[50] Zhang SP, Wang G, Zhang ZL, Wang BB, Bai JT, Wang H (2019) 3D graphene networks encapsulated with ultrathin SnS nanosheets @hollow mesoporous carbon spheres nanocomposite with pseudocapacitance-enhanced lithium and sodium storage kinetics. Small 15:1900565

[51] Yang L, Hong WW, Zhang Y, Tian Y, Gao X, Zhu YR et al (2019) Hierarchical NiS_2 modified with bifunctional carbon for enhanced potassium-ion storage. Adv Funct Mater 29:1903454

[52] Sun DF, Wang L, Li YL, Yang YX, Zhou XZ, Ma GF, Lei ZQ (2019) Confined metal sulfides nanoparticles into porous carbon nanosheets with surface-controlled reactions for fast and stable lithium-ion batteries. ChemElectroChem 6:4464–4470